CC BY

Comparative Performance of Commercial Versus Biosynthesized Chitosan-Epichlorohydrin/Kaolinite Biocomposites for Methyl Orange Removal: Box–Behnken Optimization, Adsorption Mechanism, and Density Functional Theory Calculations

Hala Benoumena[1], Ammar Zobeidi[2], Salem Atia[3], Wassima Lakhdari[4], Abderrahmene Dehliz[5], Mustapha Mounir Bouhenna[6], Mourad Mimouni[7]

[1] Pollution and waste treatment laboratory (PWTL), University of Ouargla, Algeria. benoumenahala@gmail.com
[2] Department of Chemistry, Faculty of Exact Sciences, University of El-Oued, Algeria. zobeidi.aa@gmail.com
[3] Pollution and waste treatment laboratory (PWTL), University of Ouargla, Algeria. atiassalem@gmail.com
[4] National Institute of Agronomic Research of Algeria, Touggourt, Algeria. lakhdariwassima@yahoo.fr
[5] National Institute of Agronomic Research of Algeria, Touggourt, Algeria. dahliyacine@gmail.com
[6] Center of Research in Physical and Chemical Analysis (CRAPC), Algeria. bouhenna3@yahoo.fr
[7] LEVRES Laboratory, University of El Oued, Algeria. mimouni-mourad@univ-eloued.dz

Received: 05-03-2026 **Accepted**:15-05-2026 **Published**:12-06-2026

Abstract: Water contamination by synthetic dyes poses a serious environmental threat, driving the need for affordable and efficient adsorbents. This study developed two novel biocomposites by grafting commercial chitosan (c-CTS-ECH/KC) and locally biosynthesized chitosan (b-CTS-ECH/KC) onto natural kaolinite clay from Algeria using epichlorohydrin as a crosslinking. Characterization via FTIR, BET, and EDX confirmed successful chitosan grafting and demonstrated an increase in surface area compared to raw kaolinite. Adsorption performance for methyl orange (MO) dye was optimized using response surface methodology, achieving maximum removal efficiencies of 82.6% and 80.2% for c-CTS-ECH/KC and b-CTS-ECH/KC, respectively. Kinetic studies revealed chemisorption as the rate-limiting step, while equilibrium data fitted the Langmuir model for c-CTS-ECH/KC (q_{max}: 216.92 mg/g) and the Freundlich model for b-CTS-ECH/KC (q_{max}:204.082mg/g), indicating surface heterogeneity. Thermodynamic analysis showed the adsorption was spontaneous, endothermic, and entropy-driven. Computational DFT and NBO analyses supported the experimental findings, revealing enhanced surface reactivity upon chitosan modification and strong electrostatic interactions between chitosan's electron-rich amino groups and MO's sulfonate oxygens, alongside hydrogen bonding and π–π stacking. Overall, these chitosan-modified kaolinite biocomposites demonstrate significant promise as sustainable, cost-effective adsorbents for treating dye-contaminated wastewater.

Keywords: Chitosan; Crosslinking; Kaolinite clay; Methyl orange dye; Adsorption; Box-Behnken Design; Density Functional Theory.

1. Introduction

Water pollution caused by synthetic dyes remains a major environmental and public health concern, with textile, paper, and leather industries discharging large volumes of dye-laden effluent into aquatic systems each year. Methyl orange (MO), an anionic dye widely used, is particularly problematic because of its high water solubility, resistance to biodegradation, and demonstrated toxicity toward aquatic organisms, making its removal from wastewater before discharge essential for protecting both ecosystems and human health [1,2].

Adsorption onto natural clay minerals such as kaolinite (KC) has long been recognized as a low-cost, accessible route for anionic dye removal [3], but unmodified clays generally offer limited surface charge and a narrow range of reactive functional groups, capping their adsorption capacity. Chitosan (CTS), a biopolymer rich in amino and hydroxyl groups, complements this limitation by providing abundant sites for electrostatic interaction and hydrogen bonding with anionic dyes, but its poor mechanical stability and solubility in acidic media restrict standalone use. Crosslinking chitosan with epichlorohydrin (ECH) and immobilizing it on a clay support has proven effective at overcoming both limitations simultaneously, and several recent studies have validated this strategy: CTS-ECH/KC and related clay biocomposites have been optimized through response surface methodology for the removal of reactive, azo, and basic dyes, achieving high removal efficiencies while improving reusability and structural stability [4-7].

Despite this progress, nearly all reported chitosan-clay composites rely on commercially sourced chitosan, leaving the comparative performance of locally or regionally produced chitosan largely unexamined, even though low-cost extraction of chitosan from regional biomass is well established and increasingly promoted as a sustainable alternative to imported biopolymer [8]. This gap is particularly relevant in regions such as Algeria, where valorization of locally available clay and biological raw materials for water treatment applications is gaining renewed attention [9].

With the rapid advancement of computational resources, quantum-chemical methods have become increasingly prevalent in the study of dye adsorption [10,11]. In particular, density functional theory (DFT) has proven highly effective for elucidating adsorption mechanisms and characterizing the electronic behavior of dyes in relation to adsorbent surfaces [12,13]. The reactivity descriptors derived from DFT now serve as robust tools for probing organic reactivity and intermolecular interactions [14].

The present study addresses this gap by synthesizing two epichlorohydrin-crosslinked chitosan/kaolinite biocomposites, one from commercial chitosan (c-CTS-ECH/KC) and one from chitosan synthesized locally at National Institute of Agronomic Research of Algeria INRAA Touggourt (b-CTS-ECH/KC), using kaolinite sourced from Tamanrasset, Algeria. The aim is to determine whether the locally produced chitosan performs comparably to its commercial counterpart for methyl orange removal, while applying Response Surface Methodology based on a Box-Behnken Design (RSM-BBD) to optimize adsorbent dose, pH, contact time, temperature, and chitosan loading, and to elucidate the governing kinetics, isotherms, thermodynamics, and adsorption mechanism. The materials and procedures used to synthesize, characterize, and evaluate these biocomposites are detailed in the following section. DFT calculations are applied to study to correlate experimental findings with theoretical reactivity descriptors and optimize multi-dye removal efficiency.

2. Experimental

2.1 Chemicals

Raw kaolinite clay (kaol) was sourced from Tamanrasset in southeastern Algeria. Methylene orange dye ($C_{14}H_{14}N_3NaO_3S$, MW: 327.33g/mol, λ_{max} =465 nm) is obtained from Sigma-Aldrich. Commercial Chitosan (c-CTS, deacetylation ≥75 %; medium MW) (c-CTS) was procured from Sigma-Aldrich. Synthesis (b-CTS, deacetylation ≥77 %; medium MW) (b-CTS) is obtained from INRAA Touggourt. Analytical grade reagents including hydrogen peroxide (H_2O_2), Epichlorohydrin (C_3H_5CLO), sodium acetate (CH_3COONa), acetic acid (CH_3COOH), sodium hexametaphosphate ($(NaPO_3)_6$), hydrochloric acid (HCl), and sodium hydroxide (NaOH) were supplied by Merck.

2.2 Treatment the Raw Clay

The raw clay was purified to eliminate crystalline phases and organic matter following a previously reported procedure [15-17]. Briefly, 10 g of clay was gradually introduced into 150 ml of acetate buffer solution (pH 4.8; sodium acetate/acetic acid) under continuous stirring. To remove organic impurities, 50 mL of H_2O_2 6% (v/v) was added to the suspension. The resulting mixture was transferred to a graduated cylinder and allowed to settle for approximately 8 h, after which the fraction collected at a depth of 10 cm yielded particles smaller than 2 µm. The purified clay was then recovered by vacuum filtration, thoroughly washed with distilled water serval time, and dried in an oven at 105°C for 24 h. The dried material was subsequently ground and sieved to a particle size.

2.3 Preparation the c-CTS-ECH/KC and b-CTS-ECH/KC biocomposites

The biocomposites were synthesized following the same procedure. Briefly, 1 g of chitosan flakes was dissolved in 50 mL of 5% (v/v) acetic acid solution and stirred continuously at room temperature until a homogeneous gel was obtained. Subsequently, 1 g of KC was incorporated into the gel and the mixture was maintained under vigorous stirring for 24 h at room temperature. The resulting suspension was extruded dropwise through a 10 mL syringe needle into 1000 mL of 0.5 M sodium hydroxide solution, leading to the instantaneous formation of CTS-KC beads. The obtained beads were repeatedly washed with distilled water to eliminate residual NaOH. Cross-linking was then performed by immersing the beads in 100 mL of 1% ECH solution under mild stirring in a water bath at 40°C for 2 h. The resulting c-CTS-ECH/KC and b-CTS-ECH/KC beads were subsequently washed several times with distilled water and air-dried at room temperature. It is worth noting that the clay-to-chitosan mass ratio was carefully controlled during biocomposites preparation. The biocomposites with a 50% clay content were prepared using a 1:1 (clay:chitosan) ratio, whereas those with a 25% clay content were prepared using a 1:3 (clay:chitosan) ratio.

2.4 Characterization

The crystalline structure of the samples was characterized by X-ray diffraction (XRD) analysis (Hitachi, TM3030Plus, Tabletop Microscope). Fourier transform infrared (FTIR) spectroscopy (Cary 600 Series, Agilent Technologies) was employed to identify the surface functional groups. The specific surface area, pore volume, and pore size distribution were determined from N_2 adsorption/desorption isotherms measured at 77 K using a Micromeritics ASAP 2020 analyzer, based on the Brunauer–Emmett–Teller (BET) method. The morphology and elemental composition of the samples were examined by scanning electron microscopy coupled with energy-dispersive X-ray spectroscopy (SEM-EDX) using a Hitachi TM3030Plus tabletop microscope (Hitachi, Tokyo, Japan). Dye concentrations in solution were determined by measuring absorbance at the characteristic wavelength using a UV–Visible spectrophotometer (UV–Vis). The point of zero charge (pH_{pzc}) of c-CTS-ECH/KC-25 and b-CTS-ECH/KC-25 biocomposites were determined according to the method described elsewhere [18,19].

2.5 Experimental Design

In this study, Response Surface Methodology based on Box-Behnken Design (RSM-BBD) was applied to optimize the combined effects of five independent variables on MO dye removal efficiency by c-CTS-ECH/KC and b-CTS-

ECH/KC biocomposites. The investigated parameters were: adsorbent mass (A), solution pH (B), contact time (C), temperature (D), and chitosan loading in kaolin (E). The experimental ranges and coded levels of each independent variable, established on the basis of preliminary experiments, are summarized in Table1.

To correlate the response variable with the independent parameters and predict MO dye removal efficiency, a second-order polynomial model was fitted to the experimental data according to the following equation:

$Y= \beta_0 + \sum\beta_i X_i + \sum\beta_{ii} X_i^2 + \sum\sum\beta_{ij} X_i X_j, + \varepsilon$, (1)

where: Y is an objective to optimize the response, x_i and x_j represent the response of MO dye removal, k indicates the number of variables, i and j denote the index numbers for variables, β_0 is the constant coefficient, β_i is the linear coefficient, β_{ii} is the quadratic coefficient, β_{ij} is the interaction coefficient, and ε represents a random error.

Based on the BBD design, a total of 46 experimental runs were generated, comprising three levels, five factors, and six center points, to optimize and evaluate the influence of the following independent variables on MO dye removal (%): adsorbent mass (A: 0.02–0.2 g), solution pH (B: 4–14), contact time (C: 15–75 min), temperature (D: 30–60°C), and chitosan loading in kaolin (E: 0–50%). The complete BBD experimental matrix along with the corresponding MO dye removal responses are presented in Table 1.

For each experimental run, a predetermined amount of adsorbent was introduced into 100 mL Erlenmeyer flasks containing 100 mL of MO dye solution of known initial concentration. The flasks were placed in a thermostatic water bath and agitated at a constant shaking speed of 100 rpm for the designated contact time. At the end of each experiment, the residual MO dye concentration in solution was determined by UV–Vis spectrophotometry at the maximum absorption wavelength (λ_{max} = 460 nm). The MO dye removal efficiency (R%) was subsequently calculated according to equation:

$R\% = (C0 – Ce)/C0 \times 100$, (2)

Where: C_0 and C_e represent the initial and equilibrium dye concentrations (mg/L), respectively

Table 1. Coded and actual variables with their levels in BBD

code	variable	Level 1 (+1)	Level 2 (0)	Level 3 (-1)
A	Adsorbent dose (g)	0.02	0.11	0.2
B	pH	4	7	14
C	Time (min)	15	45	75
D	Temperature (C°)	30	45	60
E	Loiding (%)	0	25	50

2.6 Batch Adsorption Studies

The adsorption of MO dye onto the c-CTS-ECH/KC and b-CTS-ECH/KC biocomposites surfaces was investigated under batch mode conditions. The optimal adsorption parameters were derived from run 29 in Table 2, which corresponded to the highest MO dye removal efficiency (%) at the following conditions: adsorbent mass of 0.11 g, solution pH of 4, temperature of 45°C, and chitosan loading of 25%. Based on these optimized conditions, a series of batch adsorption experiments were conducted by varying the initial dye concentration (50–400 mg/L) and contact time (0–180 min) to evaluate the adsorption kinetics and equilibrium behavior of the biocomposites.

The equilibrium adsorption capacity q_e (mg/g), representing the amount of MO dye adsorbed per unit mass of adsorbent at equilibrium, was calculated according to equation:

$q_e = (C_o - C_e)\, V/W$, (3)

Where: C_o and C_e are the initial and equilibrium dye concentrations (mg/L), respectively; V is the volume of the dye solution (L); and W is the mass of the adsorbent (g).

Table 2. The 5-varibles BBD matrix and experimental data for MO dye removal by c-CTS-ECH/KC-25 and b-CTS-ECH/KC-25

Run	A: Absorbent dose (g)	B: pH	C:time (min)	D: Temperature (C°)	E: c-CTS and b-CTS loading (%)	Removal (%) by c-CTS-ECH/KC	Removal (%) by b-CTS-ECH/KC
1	0.2	7	75	45	25	69.34	67.26
2	0.11	7	45	60	50	61.42	59.58
3	0.02	10	45	45	25	0	0
4	0.11	4	45	60	25	74.54	72.3
5	0.11	7	45	45	25	35.75	34.68
6	0.11	7	75	30	25	60.72	58.91
7	0.11	7	45	45	25	34.98	33.93
8	0.11	7	45	45	25	35.6	34.53
9	0.11	7	45	60	0	54.55	54.07

10	0.11	4	45	45	50	45.2	43.24
11	0.11	4	45	45	0	66.86	65.86
12	0.02	7	45	60	25	42.65	41.37
13	0.2	7	45	30	25	63.26	61.36
14	0.11	7	15	45	50	16	15.52
15	0.02	4	45	45	25	74.03	71.81
16	0.11	10	45	60	25	62.43	60.56
17	0.11	7	45	45	25	35.23	34.17
18	0.2	7	45	45	50	64.49	62.56
19	0.11	7	15	60	25	53.8	52.19
20	0.11	4	15	45	25	0.45	0
21	0.11	10	45	45	0	4.2	4.06
22	0.02	7	15	45	25	40.35	39.14
23	0.11	7	75	60	25	70.03	67.93
24	0.2	7	45	60	25	82.2	79.73
25	0.11	7	45	45	25	35.67	34.6
26	0.11	7	75	45	0	26.8	25.98
27	0.11	7	75	45	50	63.89	61.75
28	0.2	7	45	45	0	17.95	17.45
29	0.11	4	75	45	25	82.6	80.2
30	0.2	10	45	45	25	35.54	34.41
31	0.11	10	45	30	25	13.45	13.05
32	0.11	7	15	30	25	17.4	16.84
33	0.02	7	45	45	0	4.95	4.84
34	0.11	10	15	45	25	0	0
35	0.11	7	45	30	50	32.9	31.84
36	0.11	4	45	30	25	54.55	52.75
37	0.11	10	45	45	50	59.69	57.84
38	0.02	7	75	45	25	28.05	27.21
39	0.11	7	45	30	0	49.05	48.54
40	0.02	7	45	30	25	22.35	21.68
41	0.11	7	15	45	0	10.75	10.42
42	0.11	7	45	45	25	35.67	34.65
43	0.11	10	75	45	25	23.5	22.81
44	0.02	7	45	45	50	45.2	43.81
45	0.2	7	15	45	25	56.5	54.86
46	0.2	4	45	45	25	77.54	75.45

2.7 Theoretical Research DFT

The geometry of the kaolinite, chitosan monomere and MO dye were optimized using DFT, specifically at the B3LYP/6–31G(d,p), as implemented in the Gaussian 09 software [20]. From the optimized electronic configurations, a comprehensive set of global reactivity descriptors was computed, including E_{HOMO}, E_{LUMO}, E_{gap}, the electronic chemical potential (μ), chemical hardness (η), softness (S), and the electrophilicity index (ω) [11]. The chemical descriptors for biocomposites were computed using the following working expressions:

Gap energy: $E_{gap} = E_{LUMO} - E_{HOMO}$, (4)

Electronic chemical potential: $\mu = (E_{LUMO} + E_{HOMO})/2$, (5)

Chemical hardness: $\eta = (E_{LUMO} - E_{HOMO})/2$, (6)

Softness: $S = 1/\eta$, (7)

Electrophilicity: $\omega = \mu^2/2\eta$, (8)

3. Results And Discussion

3.1 Characterization

3.1.1 XRD Analysis

The XRD pattern of Kaol sample is illustrated in fig.1. It presented diffraction peaks at 2θ = 12.31, 20.04, 24.918, 35.179, 38.546, 45.505, 54.092 and 62.159°. This result indicates the dominance of Kaolinite $Al_2Si_2O_5(OH)_4$ in the sample [21,22]. A strong reflection at 2θ = 12.311° corresponding to d-spacing of 7.184Å, characteristic of kaolinite group minerals. The presence of kaolinite is further confirmed by characteristic reflections at 7.184 Å (001), 4.426 Å (020), and 1.492 Å (060) [23].

Table 3. Calculated unit cell parameters of the mineral clay

Unit cell parameter	a	b	c	β
Experimental value	5.2 A°	8.85 A°	7.18 A°	100 °
Value of the reference (file n°9009234)	5.154Å	8.942	7.391Å	β=105.046°

We see that the calculated values of unit cell parameters in table 3 are closers to the reference ones (COD 9009234), which confirm the success of our preparation protocol. In the other hand, and from the fig.1. Which present the XRD patterns of both chitosan-modified samples b-CTS-ECH/KC-25 and c-CTS-ECH/KC-25 show systematic changes compared to KC sample: both chitosan biocomposites exhibit significant reduction in peak intensities across all major reflections, indicating partial loss of crystalline ordering due to polymer intercalation [24]. Preservation of characteristic kaolinite reflections confirms that chitosan intercalation does not destroy the fundamental aluminosilicate structure. Absence of distinct chitosan crystalline reflections suggests the polymer exists in an amorphous or semi-crystalline state within the clay interlayers [25].

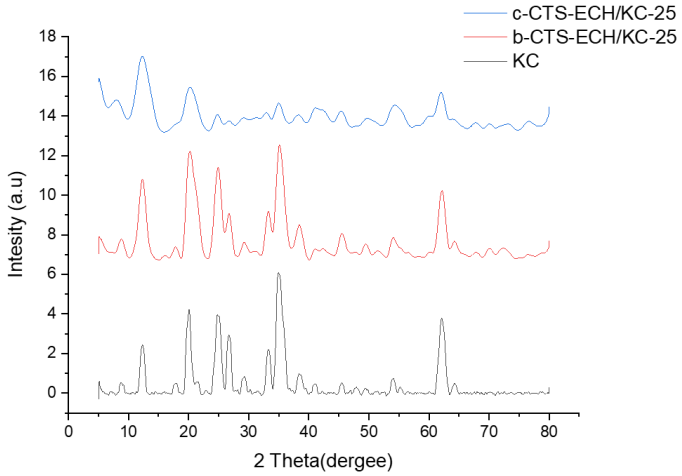

Fig .1. XRD patterns of KC and the doped clay with c-CTS-ECH/KC-25 and b-CTS-ECH/KC-25.

3.1.2 SEM & EDX Analysis

In fig. 2. (a) we present the SEM results of KC sample which reveal the characteristic morphology of natural clay minerals. The sample exhibits well-defined plate-like structures with smooth surfaces and sharp edges, typical of kaolinite's triclinic crystal system [22]. Individual kaolinite sheets appear more agglomerated compared to the b-CTS-ECH/KC-25 and c-CTS-ECH/KC-25, suggesting chitosan acts as a binding agent between particles. This is attributed to the crosslinked chitosan network formation through epichlorohydrin bridges [26]. The grain size distribution in fig.2. (a) shows that the grains have a size between 40 nm to 160nm and a middle size of 0.1µm (100nm).

In fig.2. (a) we illustrate the SEM results of c-CTS-ECH/KC-25 sample which confirm the sheet-like morphology remains more recognizable compared to b-CTS-ECH/KC-25 sample and indicating more controlled modification without excessive structural disruption.

The grain size distribution shows that the maximum of the size is under 1µm in case of the c-CTS-ECH/KC-25 sample and reach 160 nm in case of the b-CTS-ECH/KC-25 sample and the middle grains size is 60nm for both b-CTS-ECH/KC-25 and c-CTS-ECH/KC-25 samples.

The EDX analysis results presented in the same fig confirm the presence of the expected elements: C, O, Al, Si, K, and Fe, consistent with its mineralogical composition of kaolinite ($Al_2Si_2O_5(OH)_4$) [27]. Upon modification with chitosan crosslinked, several significant changes in elemental composition were observed. The relative mass percentages of Al and Si increased in both biocomposites samples (Al: from 5.61% to 11.14% and 8.22%; Si: from 5.41% to 12.98% and 9.22% for c-CTS-ECH/KC-25 and b-CTS-ECH/KC-25, respectively), while the Fe content decreased markedly (from 17.53% to 9.60% and 12.76%). This redistribution reflects the deposition of the organic chitosan layer onto the kaolinite surface, partially covering iron-bearing impurity phases while exposing the underlying aluminosilicate structure more clearness.

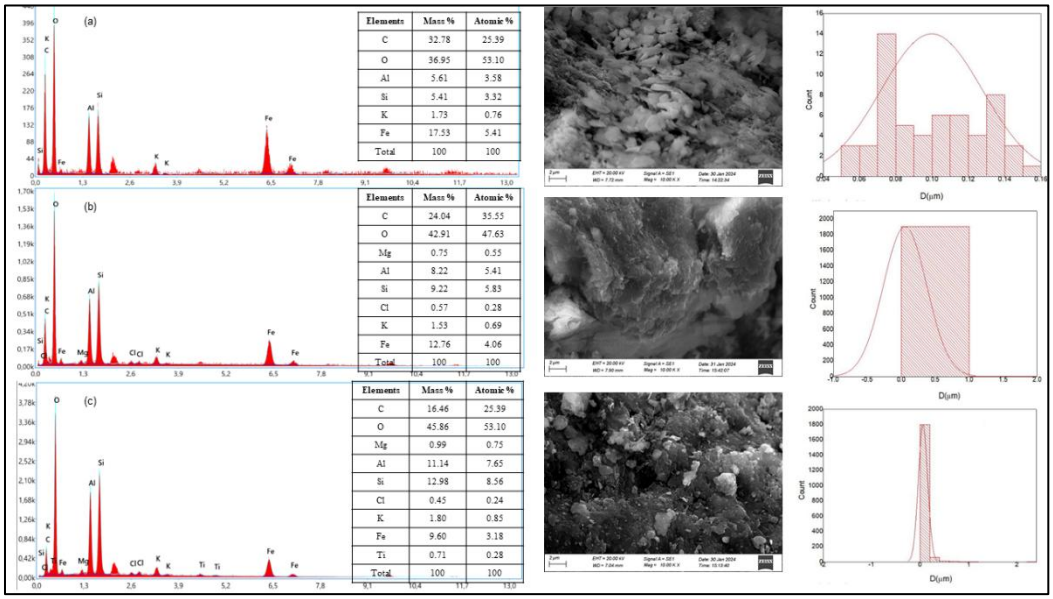

Fig.2. SEM, EDX and grain size distribution results of (a)KC, (b) b-CTS-ECH/KC-25 and, (c) c-CTS-ECH/KC-25.

3.1.3 FTIR Analysis

The FTIR spectrum in fig .3. of the KC substrate exhibits characteristic absorption bands consistent with typical aluminosilicate minerals. The broad absorption band centered at approximately 3698 and 3623 cm^{-1} is attributed to the O-H stretching vibrations [28]. The intense absorption peaks observed in the 998.9 cm^{-1} correspond to the asymmetric Si-O stretching vibrations of the tetrahedral silica sheets. Additional bands at 909 cm^{-1} are characteristic of Al-OH bending vibrations, the low-frequency region 529 cm^{-1} displays bands associated with Si-O-Si and Si-O-Al bending modes. 782.7 cm−1 for Si–O-Si inter tetrahedral bridging bonds [29-31].

FTIR spectroscopy confirmed successful chitosan integration into clay matrices for synthesis and commercial biocomposites samples. The appearance of characteristic chitosan bands at 3350-3450 cm^{-1} (N-H stretching) [31], 2850-2950 cm^{-1} (C-H stretching) [32], and 1590-1600 cm^{-1} (N-H bending) in all biocomposites spectra demonstrates effective polymer integration [33,34]. confirming that both chitosan sources provide equivalent functional group density for dye adsorption applications.

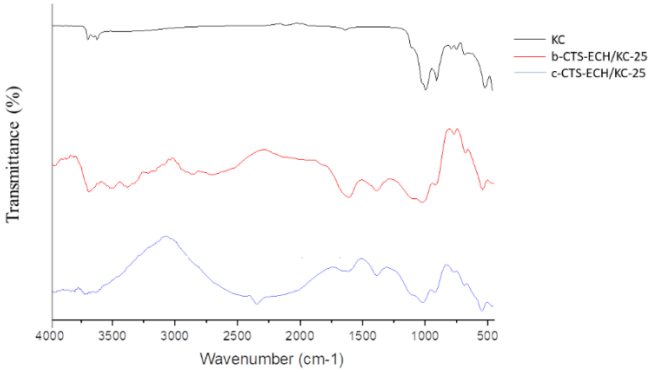

Fig .3. FTIR spectrum of KC, c-CTS-ECH/KC-25 and b-CTS-ECH/KC-25.

3.1.4 BET Surface Area and Pore Volume Analysis

Table 4. values of BET surface area and pore size

Description	BET Surface Area (m^2/g)	Total Pore Volume (cm^3/g)	Mean Pore Diameter (nm)
KC	44.06	0.164	14.74
b-CTS-ECH/KC-25	19.07	0.041	6.95

c-CTS-ECH/KC-25	19.46	0.056	8.34

The textural properties of KC, c-CTS-ECH/KC-25 and b-CTS-ECH/KC-25 were investigated by nitrogen (N_2) adsorption-desorption measurements at 77 K, and the results are summarized in Table 3. The N_2 adsorption-desorption isotherms of all synthesized materials are presented in Fig .4. The N2 physisorption isotherm of Kaol was Type II isotherm according to IUPAC classification, characteristic of non-porous or macroporous materials with unrestricted monolayer-multilayer adsorption. All chitosan-modified samples demonstrate Type IV isotherms with distinct H3-type hysteresis loops, characteristic of mesoporous materials according to IUPAC classification. [35] Transition from Type II (pristine clay) to Type IV (modified biocomposites) confirms mesopore development through chitosan intercalation and surface modification. The consistent H3-type hysteresis across all modified samples indicates the slit-shaped pore geometry typical of layered materials. Pore network effects due to chitosan bridging between clay layers and ink-bottle pore formation where chitosan partially blocks pore entrances [36].

The BET surface area analysis revealed significant textural modifications upon chitosan incorporation into the kaolinite clay matrix. The KC exhibited a BET surface area of 44.06 m^2/g, with a total pore volume of 0.164 cm^3/g and a mean pore diameter of 14.74 nm. which serves as the baseline for comparison. Upon chitosan modification, substantial reductions in surface area were observed across all biocomposites samples.

At 25% chitosan loading, both b-CTS-ECH/KC-25 (≈19.07 m^2/g) and c-CTS-ECH/KC-25 (≈19.46 m^2/g) demonstrated approximately 57% reduction in BET surface area compared to KC. The total pore volume also decreased significantly from 0.164 to 0.041 and 0.056 cm^3/g for b-CTS-ECH/KC-25 and c-CTS-ECH/KC-25 respectively, this similarity in values suggests that both chitosan types exhibit comparable surface coverage, the partial blocking and loading of kaolinite's pores and surface sites by chitosan chains. confirms the loading-filling mechanism of chitosan within the clay matrix. and intercalation behavior within the kaolinite interlayer structure at equivalent loading concentrations [37].

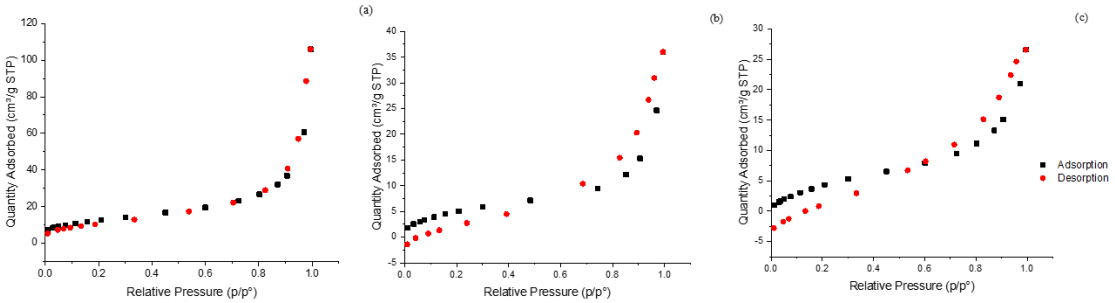

Fig.4. N2 adsorption/desorption isotherms of (a) KC, (b) c-CTS-ECH/KC-25 and (c) b-CTS-ECH/KC-25.

3.2 BBD Model Analysis

The individual and synergistic effects of critical operational parameters including c-CTS-ECH/KC-25 and b-CTS-ECH/KC-25 dosage (A), solution pH (B), contact time (C), temperature (D), and initial CS loading (E), on methylene orange (MO) removal efficiency were systematically investigated using BBD-RSM. The statistical significance and adequacy of the developed model were evaluated through ANOVA of MO removal data. the result of both biocomposites in table 2.

By the BBD model the F-value of c-CTS-ECH/KC-25 and b-CTS-ECH/KC-25 was 5.08 and 5.00, respectively and the p-value of <0.0001 for the both corposants. this result is indicated that BBD model was statistically significant for removal MO by both corposant [38] .the coefficient determination R^2 was approximately the same value 0.80 for c-CTS-ECH/KC-25 and 0.7999 for b-CTS-ECH/KC-25 indicates a good correlation between the observed and predicted values of MO dye removal.

The significance of the BBD model was determined by its p-value. Factors with p-values less than 0.05 are considered significant. The ANOVA reveals that the term for the both biocomposites A, B, C, D, E, BC, BE and D^2 were significant for the removal of MO dye.

Table 5. Analysis of variance (ANOVA) of c-CTS-ECH/KC-25 for the removal dye MO

Source	Sum of Squares	df	Mean Square	F-value	p-value	
Model	20572.58	20	1028.63	5.08	< 0.0001	significant
A-m	2736.34	1	2736.34	13.51	0.0011	
B-pH	4794.18	1	4794.18	23.68	< 0.0001	
C-time	3297.06	1	3297.06	16.28	0.0005	

D-T	2207.59	1	2207.59	10.90	0.0029	
E-loading	1476.10	1	1476.10	7.29	0.0123	
AB	256.48	1	256.48	1.27	0.2711	
AC	158.00	1	158.00	0.7803	0.3855	
AD	0.4624	1	0.4624	0.0023	0.9623	
AE	9.89	1	9.89	0.0488	0.8269	
BC	859.96	1	859.96	4.25	0.0499	
BD	210.11	1	210.11	1.04	0.3181	
BE	1488.03	1	1488.03	7.35	0.0120	
CD	183.47	1	183.47	0.9060	0.3503	
CE	253.45	1	253.45	1.25	0.2739	
DE	132.48	1	132.48	0.6542	0.4262	
A^2	380.21	1	380.21	1.88	0.1828	
B^2	52.33	1	52.33	0.2584	0.6157	
C^2	37.92	1	37.92	0.1873	0.6689	
D^2	1753.68	1	1753.68	8.66	0.0069	
E^2	27.48	1	27.48	0.1357	0.7157	
Residual	5062.33	25	202.49			
Cor Total	25634.91	45				

Table 6. Analysis of variance (ANOVA) of b-CTS-ECH/KC-25 for the removal dye MO

Source	Sum of Squares	df	Mean Square	F-value	p-value	
Model	19400.02	20	970.00	5.00	0.0001	significant
A-m	2581.15	1	2581.15	13.30	0.0012	
B-ph	4518.53	1	4518.53	23.28	< 0.0001	
C-time	3110.29	1	3110.29	16.02	0.0005	
D-T	2087.58	1	2087.58	10.75	0.0031	
E-loading	1312.61	1	1312.61	6.76	0.0154	
AB	236.70	1	236.70	1.22	0.2800	
AC	147.99	1	147.99	0.7624	0.3909	
AD	0.4356	1	0.4356	0.0022	0.9626	
AE	9.42	1	9.42	0.0486	0.8274	
BC	823.40	1	823.40	4.24	0.0500	
BD	195.44	1	195.44	1.01	0.3253	
BE	1459.24	1	1459.24	7.52	0.0111	
CD	173.32	1	173.32	0.8929	0.3537	
CE	235.16	1	235.16	1.21	0.2815	
DE	123.32	1	123.32	0.6353	0.4329	
A^2	355.47	1	355.47	1.83	0.1881	
B^2	47.46	1	47.46	0.2445	0.6253	
C^2	38.90	1	38.90	0.2004	0.6583	
D^2	1677.01	1	1677.01	8.64	0.0070	
E^2	21.87	1	21.87	0.1127	0.7399	
Residual	4852.81	25	194.11			
Cor Total	24252.83	45				

Model terms with P-values < 0.05 were excluded from the second-order polynomial equation to optimize model fit. The relationship between the examined parameters and the response (MO dye removal) was then established using the calculated equation (12) and equation (13) for c-CTS-ECH/KC-25 and b-CTS-ECH/KC-25 respectively:

MO removal = +35.48 +13.08A -17.31B +14.36C +11.75D +9.61E +8.01 AB+ 6.29AC -0.34 AD +1.57 AE -14.66BC +7.25 BD +19.29BE -6.77 CD +7.96 CE +5.76 DE +6.60 A^2 +2.45B^2 -2.08 C^2 +14.18 D^2 -1.77 E^2, (9)

MO removal = +34.43 +12.70A -16.81B +13.94C +11.42D +9.06E +7.69AB +6.08AC -0.33AD +1.54AE -14.35BC +6.99BD +19.10BE -6.58CD +7.67CE +5.55DE +6.38A^2 +2.33B^2 -2.11C^2 +13.86D^2 -1.58E^2, (10)

Model validity was further confirmed through graphical analysis. The normal probability plot of residuals fig.5. shows that data points are closely aligned along a straight line, indicating a normal distribution of residuals and confirming the efficiency of model assumptions [39]. Additionally, the predicted and actual plot reveals a strong agreement

between predicted and experimental MO dye removal values (%), further demonstrating the statistical reliability of the model [40].

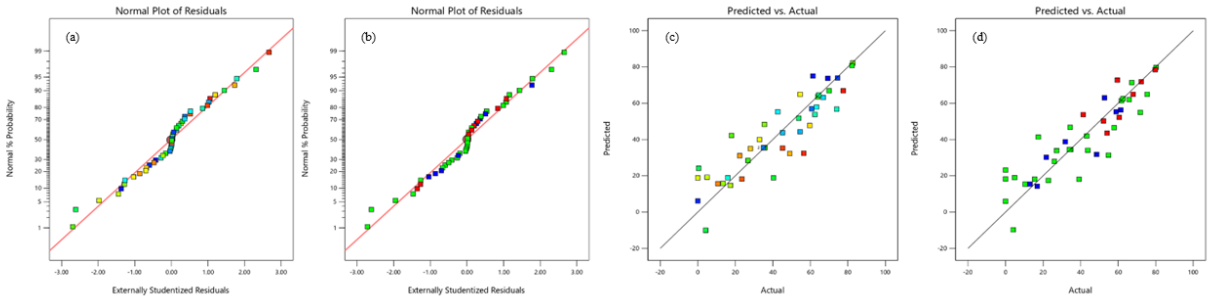

Fig.5. (a) Normal probability plot of residuals for c-CTS-ECH/KC-25 to MO dye removal and(b) for b-CTS-ECH/KC-25, (c) plot of the relationship between the predicted and actual values for c-CTS-ECH/KC-25 of MO dye removal (%) and (d) for b-CTS-ECH/KC-25

The interaction effects between pairs of independent variables on MO dye removal were evaluated, including the interaction between solution pH (B) and time (C) was statistically significant for the both corposant c-CTS-ECH/KC-25 and b-CTS-ECH/KC-25 (p-value = 0.0499) (p-value = 0.0500) on the removal of the MO dye. The other factors were constants at (adsorbent dose 0.11g, temperature 45 C° and CS loading 25%). 3D response surface is shewing in fig.6. indicating the interaction between solution pH and contact time for the both biocomposites. The pH_{pzc} are in fig.7. were 7.1 and 7 for the c-CTS-ECH/KC-25 and b-CTS-ECH/KC-25 respectively. The model identifies a pronounced region of maximum efficiency (>80%) under acidic conditions (pH =2-6), a finding directly attributable to the biocomposites pH_{pzc}, which fosters a protonated, positively charged surface conducive to electrostatic attraction with the anionic dye.

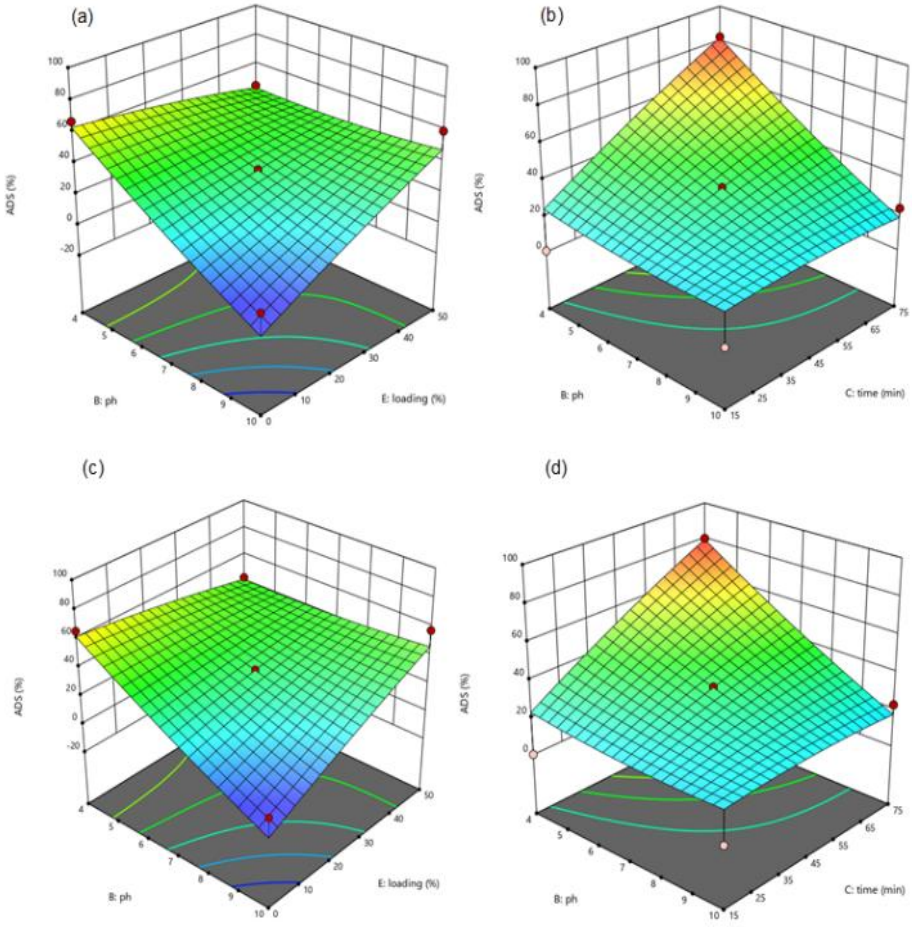

Fig.6. The 3D surface plot displays (a) interaction between the pH and c-CTS-ECH/KC-25 loading, (b) shows interaction between the contact time and the pH for c-CTS-ECH/KC-25, (c) interaction between pH and b-CTS-ECH/KC-25 loading, (d) shows interaction between the contact time and the pH for b-CTS-ECH/KC-25.

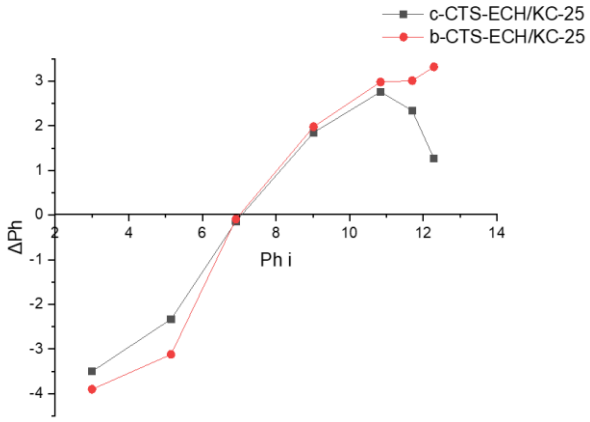

Fig.7. Determination of pH_{pzc} for c-CTS-ECH/KC-25 and b-CTS-ECH/KC-25 composite.

At pH values below this point, the surface was protonated. The amino groups (-NH_2) from chitosan are protonated to ammonium groups (-NH_3^+). Simultaneously, the kaolinite structure contributes significantly: the aluminol groups (Al-OH) at the edges of the kaolinite sheets are preferentially protonated to Al-OH_2^+ under acidic conditions [41]. The adsorption mechanism is thus a synergistic, electrostatic attraction between these collectively generated positive sites on the biocomposites and the sulfonate group (-SO_3^-) of the anionic MO dye. This can be represented by:

Protonation of the biocomposites Surface:

Chitosan Component: Chitosan-NH_2 + H^+ → Chitosan-NH_3^+, (11)

Kaolinite Component: ≡Al-OH + H^+ → ≡Al-OH_2^+ (Major contributor), (12)

≡Si-OH + H^+ → ≡Si-OH_2^+ (Minor contributor), (13)

Electrostatic Adsorption of Methyl Orange:

[biocomposites-NH_3^+ / biocomposites-Al-OH_2^+] + ^-O_3S-MO → biocomposites$^+\cdots{}^-O_3S$-MO, (14)

The interaction between solution pH (B) and loading (E) was statistically significant for the both corposant c-CTS-ECH/KC-25 and b-CTS-ECH/KC-25 (p-value = 0.0120) (p-value = 0.011) on the removal of the MO dye. at constants factors (adsorbent dose 0.11g, temperature 45 C° and time 45 min).

The response surface analysis for the interaction between solution pH and chitosan loading reveals a critical synergy conducting the adsorption efficiency of the MO dye. A pronounced region of maximum adsorption is observed under acidic conditions (pH ~4–6.5) and at intermediate chitosan loadings (~25–40%), that confirm the essential role of electrostatic attraction between the protonated adsorbent surface and the anionic dye. This performance optimum is attributed to the balanced contribution of functional groups, where chitosan's ammonium (–NH_3^+) groups and kaolinite's protonated aluminol (Al–OH_2^+) edges act cooperatively. Beyond ~40% chitosan loading, a marked decrease in adsorption capacity occurs, consistent with BET analysis that confirmed severe surface area reduction and pore blockage at high chitosan content. This decline indicates that excessive chitosan forms a non-porous polymer layer, smothering the clay's active sites and hindering dye diffusion. Thus, the optimal adsorption arises from a compromise—sufficient chitosan to impart active sites, without compromising the structural properties of the kaolinite scaffold.

3.3 Adsorption Kinetics

The kinetic adsorption behavior of methylene orange (MO) dye was investigated as a function of initial dye concentration and contact time for b-CTS-ECH/KC-25 and c-CTS-ECH/KC-25 adsorbents, as illustrated in fig.8. These experiments were performed under controlled conditions with fixed parameters: adsorbent dosage of 0.1 g, solution pH of 4 and temperature of 45°C.

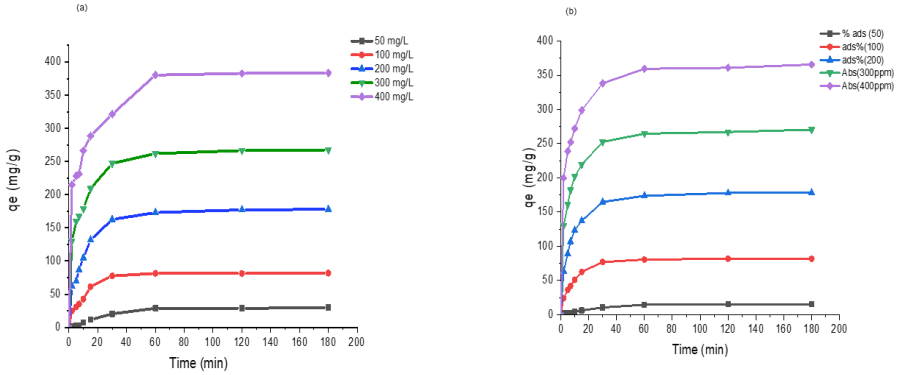

Fig.8. effect of contact time (a) c-CTS-ECH/KC-25, (b) b-CTS-ECH/KC-25 adsorption at different initial concentrations of MO.

The adsorption capacity of c-CTS-ECH/KC-25 biocomposites exhibited a significant increase from 29.8 mg/g to 356.6 mg/g when the initial MO dye concentration was elevated from 50 mg/L to 400 mg/L. This enhanced adsorption performance can be attributed to the establishment of a steeper concentration gradient, which intensifies the mass transfer driving force facilitating the migration of MO molecules to the available active sites within the c-CTS-ECH/KC-25 biocomposites matrix [41].

To characterize the adsorption kinetics of MO dye on b-CTS-ECH/KC-25 and c-CTS-ECH/KC-25 biocomposites, pseudo-first-order (PFO) and pseudo-second-order (PSO) kinetic models were applied. The non-linear mathematical formulations of PFO [42] and PSO [43] Eqs. 15 and 16, respectively, as follows:

$q_t = (1\text{-}\exp -^{k1t})$, (15)

$q_t = q^2_e k_2 t/(1+q_e k_2 t)$, (16)

where: q_t (mg/g) is the amount of MB dye adsorbed at time t (min), k_1 (1/min) is the rate constant of PFO, k_2 (g/mg.min) is the rate constant of PSO.

Table 7. PFO and PSO kinetic parameters MO adsorption on c-CTS-ECH/KC-25 composite

c-CTS-ECH/KC-25		PFO parameters for MO adsorption			PSO parameters for MO adsorption		
C_0 (ppm)	q_e (exp)	q_t (cal)	K_1	R^2	q_e (cal)	k_2	R^2
50	29.824	28.685	0.029	0.992	31.857	0.003	0.984
100	81.912	85.661	0.094	0.990	85.690	0.002	0.994
200	178.000	156.765	0.078	0.989	183.824	0.001	0.998
300	267.412	160.650	0.068	0.995	272.480	0.001	0.999
400	357.559	203.772	0.063	0.960	362.319	0.001	0.999

Table 8. PFO and PSO kinetic parameters MO adsorption on b-CTS-ECH/KC-25 composite

b-CTS-ECH/KC-25		PFO parameters for MO adsorption			PSO parameters for MO adsorption		
C_0 (ppm)	q_e(exp)	q_e (cal)	K_1	R^2	qe (cal)	k_2	R^2
50	30.97	30.766	0.0393	0.981	36.590	0.001	0.958
100	81.74	63.685	0.072	0.977	83.822	0.015	0.998
200	178.44	101.576	0.047	0.967	182.481	0.034	0.999
300	270.47	154.869	0.066	0.959	273.973	0.072	0.999
400	365.68	218.908	0.082	0.921	370.370	0.106	0.999

The kinetic parameters and correlation coefficients (R^2) for both PSO and PFO models are summarized in Table 7 and 8. The adsorption kinetics of MO dye onto b-CTS-ECH/KC-25 and c-CTS-ECH/KC-25 surfaces were best described by the PSO model, as evidenced by higher R^2 values and closer agreement between calculated equilibrium adsorption capacity q_e (cal) and experimental values q_e (exp) compared to the PFO model. Therefore, the adsorption mechanism of MO dye onto b-CTS-ECH/KC-25 and c-CTS-ECH/KC-25 biocomposites follows pseudo-second-order kinetic. Adsorption on chitosan-modified surfaces occurs through electrostatic attraction to protonated amino groups (NH_3^+) at pH < 6.5 [27,44].

3.4 Adsorption Isotherm

Adsorption isotherms constitute essential tools for explanation the nature of adsorbate-adsorbent interactions at equilibrium conditions. To evaluate the binding affinity and adsorption capacity of c-CTS-ECH/KC-25 and b-CTS-ECH/KC-25 composite for MO dye removal, three classical isotherm models were applied in their non-linear forms: Langmuir [45], Freundlich [46], and Temkin [47] models, mathematically represented by Eqs (17-19):

$C_e/q_e = q_{max}K_aC_a/ (1+ K_aC_a)$, (17)

$qe = K_fC_e^{1/n}$, (18)

$q_e = (RT/b_t) \ln(K_TC_e)$, (19)

Where: q_e (mg/g) is the amount of MO dye adsorbed per unit of the adsorbent, C_e (mg/L) is the concentration of MO dye at the adsorption equilibrium, q_{max} (mg/g) is the maximum amount adsorbed, and K_a (L/mg) is the Langmuir isotherm constant. K_f(mg/g) $(L/mg)^{1/n}$ and n are the Freundlich isotherm constants. K_T (L/mg) is the Temkin isotherm constant, and b_T (J/mol) is the heat of adsorption; T (K) is the temperature in Kelvin, and R (8.314J/mol K) is the gas constant.

Table 9. Parameters of the Langmuir, Freundlich and Temkin isotherm models for MO adsorption on CSC-ECH/Kaol-25 and CSS-ECH/Kaol-25 composite at 45 °C

Isotherm model	results	c-CTS-ECH/KC-25	b-CTS-ECH/KC-25
Langmuir	q_{max} (mg/g) K_L (L/mg) R^2	216.92 0.044 0.956	204.082 0.021 0.806
Freundlish	K_f (mg/g) (L/mg) $^{1/n}$ n R^2	42.473 3.384 0.847	2.288 1.156 0.979
Temkin	K_T (L/mg) b_t (J/mol) R^2	0.742 67.023 0.8612	0.088 35.473 0.923

Comparative analysis for describing the adsorption equilibrium of MO dye onto the b-CTS-ECH/KC-25 composite surface from results in (table 9). of the correlation coefficients (R^2) indicated that the Freundlich isotherm model provided the best fit, indicating the multilayer adsorption of the dye onto the heterogeneous surface, while the c-CTS-ECH/KC-25 follows Langmuir isotherm, indicating the monolayer adsorption of dye This indicates that MO dye molecules establish a monolayer covering on the uniform surface of the adsorbent [48].

The q_{max} of the c-CTS-ECH/KC-25, b-CTS-ECH/KC-25 for MO dye was 216.92 and 204.082 mg/g at 45 °C. For c-CTS-ECH/KC-25 higher deacetylation degree provides more amino groups, leading to stronger electrostatic interactions and higher capacity. The lower adsorption capacity compared to commercial is due to the more variable deacetylation degree results in reduced amino group availability and heterogeneous adsorption behavior [49,50].

The q_{max} of b-CTS-ECH/KC-25 and c-CTS-ECH/KC-25 biocomposites were compared with others adsorbents for dyes removal, as presented in Table 10. The comparative analysis demonstrates that b-CTS-ECH/KC-25 and c-CTS-ECH/KC-25 biocomposites exhibit competitive adsorption performance, indicating their potential as effective materials for the removal of organic dye contamination in aqueous environments.

Table 10. Comparative of adsorption capacity of MO by various adsorbent

Adsorbents	q_{max}(mg/g)	reference
chitosan-zeolites	500	[51]
Chitosan–iron(III) crosslinked	361.9	[52]
CHS-ECH/ZL composite	156.1	[53]
Chitosan/Analcime Clay	129.87	[16]
chitosan/Al_2O_3/magnetic iron oxide	417	[54]
Chitosan- epichlorohydrin/TiO2 nanocomposite	210	[55]
goethite impregnated with chitosan beads	84	[56]
chitosan/organic rectorite-Fe3O4	24.69	[57]
c-CTS-ECH/KC-25	216.92	This study
b-CTS-ECH/KC-25	204.082	This study

3.5 Thermodynamic Study

The thermodynamic parameters were calculated to investigate the adsorption process of MO onto the c-CTS-ECH/KC and b-CTS-ECH/KC surface in terms of feasibility and spontaneity, as well as to determine the degree of randomness at the solid/liquid interface. The adsorption thermodynamic parameters, namely the Gibbs free energy change (ΔG°), entropy change (ΔS°), and enthalpy change (ΔH°), were obtained using the following Eqs. (20 - 22) [58].

$\Delta G° = -RT\ln K_d$, (20)

$k_d = q_e/C_e$, (21)

$\ln k_d = \Delta S°/R - \Delta H°/RT$, (22)

Thermodynamic parameters (ΔH˚ and ΔS˚) obtained from the $\ln K_d$ against (1/T), where the slope indicates ΔH˚ and the intercept signifies ΔS˚ in Fig.9.

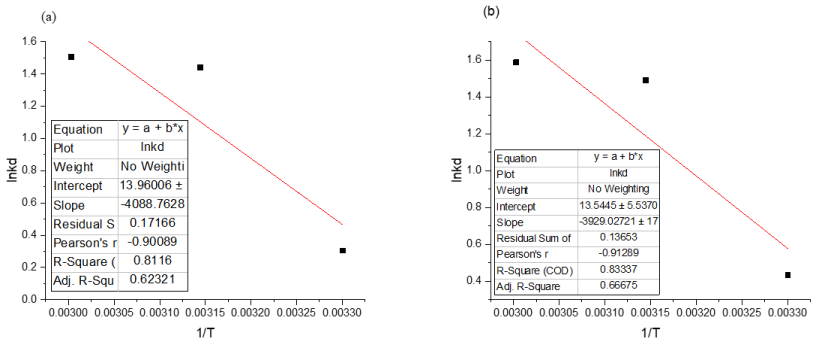

Fig.9. Van't Hoff plot for MO adsorption onto (a) b-CTS-ECH/KC-25 and (b) c-CTS-ECH/KC-25.

The thermodynamic parameters for MO dye adsorption onto b-CTS-ECH/KC-25 and c-CTS-ECH/KC-25 are summarized in Table 11 and 12. The negative values of ΔG° confirm that the adsorption process is thermodynamically spontaneous and becomes more favorable with increasing temperature. The positive ΔH° demonstrates the endothermic nature of the adsorption process, indicating that higher temperatures promote MO dye uptake onto the composite surface [42]. Moreover, the positive ΔS° reflects an increase in randomness and disorder at the solid–liquid interface during the adsorption process [53].

Table 11. Thermodynamic parameters for the adsorption of MO dye on c-CTS-ECH/KC-25

Temp (°C)	Temp (K)	ΔG (kj.mol-1)	K_d	ΔH (Kj/mol)	ΔS (Kj/mol k)
30	303	-1.455	1.543	32.666	0.113
45	318	-3.144	4.440		
60	333	-4.833	4.893		

Table 12. Thermodynamic parameters for the adsorption of MO dye on b-CTS-ECH/KC-25

Temp (°C)	Temp (K)	ΔG (kj.mol-1)	k_d	ΔH (Kj/mol)	ΔS (Kj/mol k)
30	303	-1.173	1.356	33.994	0.116
45	318	-2.914	4.223		
60	333	-4.655	4.502		

3.6 Adsorption Mechanism of MO on CTS-ECH/KC

The adsorption mechanism of MO dye onto the CTS-ECH/KC surface was proposed based on the effect of solution pH, and the point of zero charge (pH_{pzc}). As shown in Fig. 10, several simultaneous interactions govern the uptake of MO onto the composite. At pH below the pH_{pzc} of CTS-ECH/KC, the protonated amine groups ($–NH_3^+$) of chitosan interact electrostatically with the anionic sulfonate group ($–SO_3^-$) of MO, while the negatively charged $Si–O^-$ basal face of kaolinite attracts the cationic $–N^+(CH_3)_2$ end of the dye [59]. Hydrogen bonding constitutes a secondary interaction mechanism, involving the –OH and $–NH_2$ groups of chitosan, and the Si–OH/Al–OH edge sites of kaolinite, all acting as hydrogen bond donors toward the azo (–N=N–) and sulfonate groups of MO, along with Yoshida hydrogen bonding between surface hydroxyl (-OH) groups and the MO aromatic ring [60,16]. Furthermore, π–π stacking interactions between the aromatic glucosamine rings of chitosan and the benzene rings of MO contribute to the overall adsorption [13].

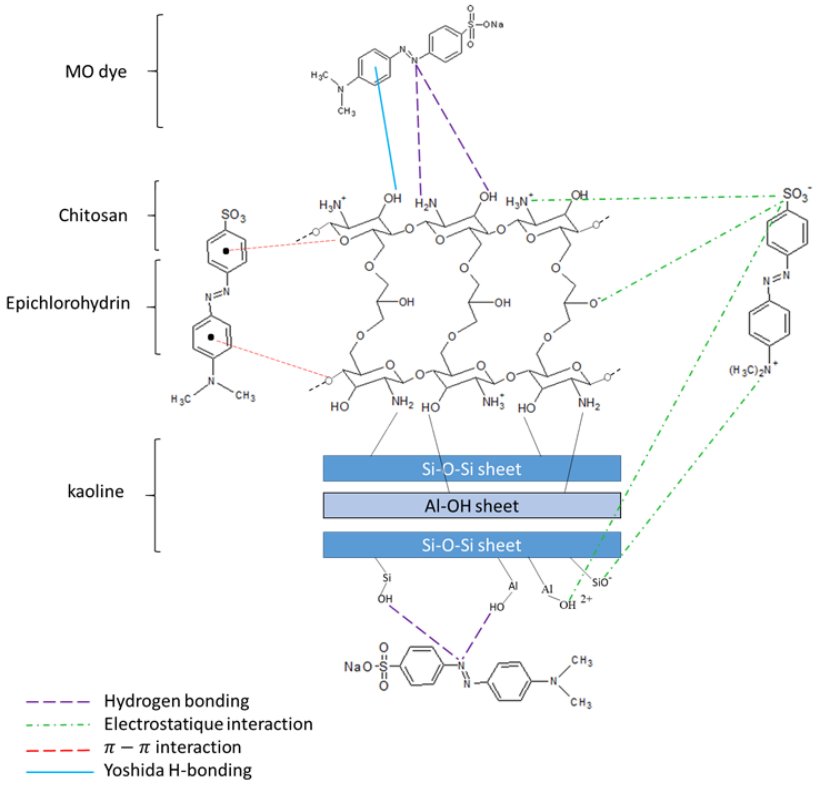

Fig. 10. Illustration of the possible interactions between CTS-ECH/KC composite surface and methyl orange (MO) dye, including electrostatic attractions, hydrogen bonding interactions, and π–π interactions.

3.7 Theoretical Study

3.8.1 HOMO and LUMO Calculation

Density Functional Theory (DFT) calculations were performed using the Gaussian 09 software. The electronic structure of three isolated systems was investigated: the kaolinite clay composition ($Al_2Si_2O_9H_4$, 17 atoms), the chitosan monomer (D-glucosamine, $C_6H_{13}NO_5$, 25 atoms), and methyl orange dye ($C_{14}H_{15}N_3O_3S$, 34 atoms). All calculations employed the Becke three-parameter Lee–Yang–Parr hybrid exchange-correlation functional (B3LYP) with the 6-31G(d,p) basis set for organic molecules (chitosan and methyl orange) and 6-31G(d) for the kaolinite mineral, consistent with established protocols for clay mineral DFT modelling.

Table 13. Calculated electronic properties of kaolinite, chitosan monomer, and methyl orange at B3LYP/6-31G(d,p) level

property	Kaolinite	Chitosan	Methyl Orange
E_{HOMO} (eV)	-7.396	-6.409	-5.475
E_{LUMO} (eV)	-2.511	+1.225	-2.327
E_{gap} (eV)	4.884	7.633	3.147
IP(eV)	7.396	6.409	5.475
EA(eV)	2.511	-1.225	2.327
Chemical potential (eV)	-4.953	-2.592	-3.901
Chemical handness	2.442	3.817	1.574
Electrophilicity (eV)	5.024	0.880	4.835

The HOMO energy of kaolinite (E_{HOMO} = −7.396 eV) is deeply negative, reflecting a tightly held electron density and a chemically inert surface character. The energy gap (E_{gap} = 4.884 eV) and high chemical hardness (η = 2.442 eV) are consistent with kaolinite being an electrical insulator. These descriptors confirm that the bare clay surface offers limited electronic interaction sites for the anionic dye.

Upon modification with chitosan, the composite introduces frontier orbital energies characteristic of the glucosamine monomer: E_{HOMO} = −6.409 eV, which is 0.987 eV higher (less negative) than kaolinite alone. This energy shift signifies that the chitosan-modified surface possesses a more accessible electron density — a prerequisite for stronger donor–acceptor interactions with the dye molecule. The markedly lower electrophilicity of chitosan (ω = 0.880 eV, versus 5.024 eV for kaolinite) further confirms that chitosan acts primarily as an electron-donating component in the composite, while kaolinite provides the structural support and Lewis acid Al/Si sites [13].

the HOMO energy of chitosan (−6.409 eV) lies above the LUMO energy of methyl orange (−2.327 eV), satisfying the fundamental frontier molecular orbital criterion for favorable donor–acceptor interaction [14]: the electron density donated by chitosan's $-NH_2$ group can be accepted by the electron-deficient azo and sulfonate groups of methyl orange. This finding provides a quantum-chemical basis for the superior adsorption performance of the c-CTS-ECH/KC and b-CTS-ECH/KC biocomposites observed experimentally.

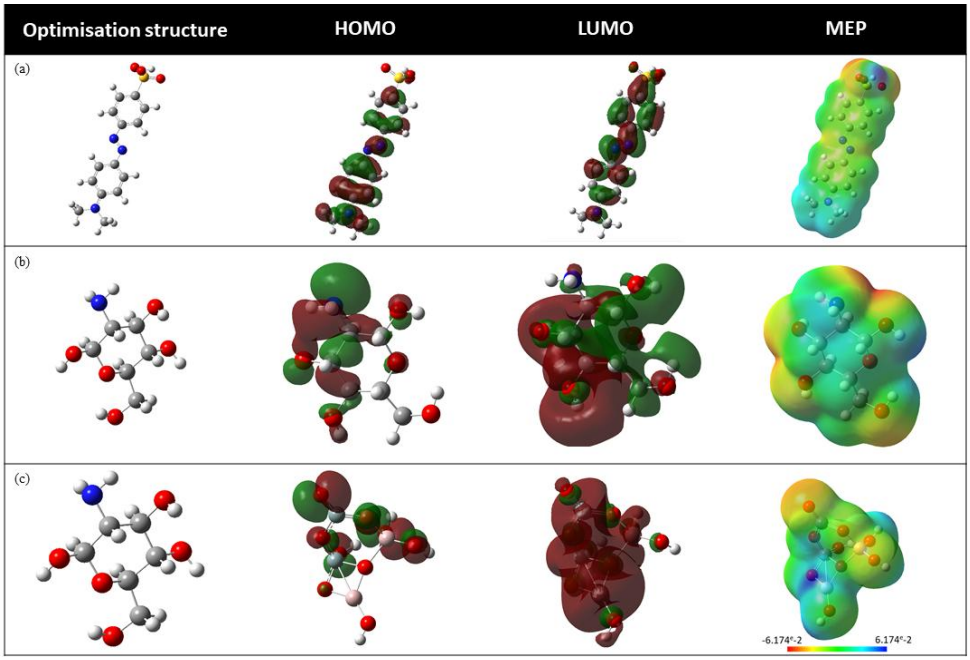

Fig.11. Optimization geometry and Visualization of the energy gap between the Highest Occupied Molecular Orbital (HOMO) and Lowest Unoccupied Molecular Orbital (LUMO), with the Molecular Electrostatic Potential (MEP) for Methyl Orange (a) Kaolinite (b) and Chitosan (c).

3.8.2 The Naturel Band Orbital (NBO) Charge Analysis

The nitrogen atom of chitosan's $-NH_2$ group carries a NBO charge of − 0.891 e, the most electron-rich site across all three molecules. At acidic pH, protonation of this nitrogen generates $-NH_3^+$, creating a positive charge center that is electrostatically complementary to the sulfonate oxygen's of methyl orange (qO = − 0.916 to − 0.946 e). The simultaneous partial positive charges on the Al surface sites (qAl = +1.982 to +2.042 e) and Si sites (qSi = +2.233 to +2.397 e) of kaolinite provide additional Lewis acid–base interaction sites with the electron-rich sulfonate group [11]. These charge distributions are fully consistent with the electrostatic mechanism proposed in Eq. 11–14. The hydroxyl protons of chitosan (qH = +0.484 to +0.486 e) and kaolinite surface OH groups (qH = +0.491 to +0.541 e) act as H-bond donors. The sulfonate oxygen's of methyl orange (q = −0.916 to −0.946 e) and its azo nitrogen's (qN = −0.190 to −0.419 e) provide complementary H-bond acceptor sites. The strong charge complementarity between these atoms confirms that hydrogen bonding constitutes a significant secondary interaction mechanism. The aromatic carbons of methyl orange carry partial negative NBO charges (qC = −0.181 to −0.343 e), consistent with an electron-rich π system available for face-to-face stacking with the glucosamine ring system of chitosan [61,62].

4. Conclusions

This study synthesized and characterized two epichlorohydrin-crosslinked chitosan/kaolinite biocomposites, c-CTS-ECH/KC from commercial chitosan and b-CTS-ECH/KC from chitosan synthesized locally at INRAA Touggourt, and evaluated their performance for methyl orange dye removal. Characterization confirmed that the kaolinite framework remained intact after modification, with chitosan grafted in an amorphous form binding the clay platelets, and that the material shifted from a non-porous Type II isotherm to a mesoporous Type IV structure with H3-type hysteresis, despite reduced surface area from pore filling by the biopolymer.

Box-Behnken optimization identified adsorbent dose, pH, contact time, temperature, and chitosan loading, along with pH-time and pH-loading interactions, as the dominant factors governing removal. Under optimized conditions (0.11 g, pH 4, 75 min, 45 °C, 25% loading), maximum removal efficiencies of 82.6% and 80.2% were achieved for c-CTS-ECH/KC-25 and b-CTS-ECH/KC-25, respectively. Adsorption followed pseudo-second-order kinetics for both materials, while equilibrium data fit the Langmuir isotherm for c-CTS-ECH/KC-25 (q_{max} = 216.92 mg/g, monolayer) and the Freundlich isotherm for b-CTS-ECH/KC-25 (q_{max} = 204.08 mg/g, multilayer). Thermodynamic analysis confirmed a spontaneous, endothermic process with increased interfacial disorder, and the proposed mechanism combined electrostatic attraction, hydrogen bonding, and π–π stacking between the composite surfaces and the MO sulfonate moiety.

These results show that b-CTS-ECH/KC, built entirely from Algerian raw materials, performs comparably to its commercial counterpart and is competitive with other adsorbents reported, positioning locally synthesized chitosan as a credible, lower-cost substitute for clay-based composite design relevant to affordable water treatment in chitosan-producing regions.

Overall, epichlorohydrin-crosslinked chitosan/kaolinite biocomposites, whether commercial or locally sourced, emerge as effective, scalable candidates for dye-contaminated wastewater remediation, with b-CTS-ECH/KC standing out as a sustainable, regionally viable alternative warranting further validation at larger scales.

DFT analysis confirms that chitosan-functionalized kaolinite exhibits enhanced electronic reactivity for methyl orange adsorption, as reflected by increased HOMO energy, favorable frontier orbital overlap, and NBO-derived electrostatic/hydrogen-bonding interactions—all consistent with the experimental kinetic and thermodynamic data.

ACKNOWLEDGMENTS

The authors would like to thankthe Biopesticides Laboratory of INRAA (Touggourt) for UV-Vis analysis as well as for providing chemicals and equipment used in this study and the Research Center in Physico-Chemical Analysis (CRAPC) for SEM, EDX, XRD, and BET analyses, the LERVES Laboratory for FTIR analysis.

FUNDING

The authors did not receive support from any organization for the submitted work.

COMPLIANCE WITH ETHICAL STANDARDS

This article does not contain any studies with human participants or animals performed by any of the authors.

CONFLICT OF INTEREST

The authors declare that they have no conflict of interest.

5. Refernces

1. M. M. Haque, M. A. Haque, M. K. Mosharaf and P. Marcus, Saudi J. Biol. Sci. 28 (2020). https://doi.org/10.1016/j.sjbs.2020.11.012
2. L. Wu, X. Liu, G. Lv, R. Zhu, L. Tian, M. Liu, Y. Li, W. Rao, T. Liu and L. Liao, Sci. Rep. 11, 10640 (2021). https://doi.org/10.1038/s41598-021-90235-1
3. A. Farhan, A. Ismail and B. Abed, J. Eng. Sci. Technol. 16, 1588 (2021).
4. F. Marrakchi, B. H. Hameed and E. Hummadi, Int. J. Biol. Macromol. 163 (2020). https://doi.org/10.1016/j.ijbiomac.2020.07.032
5. A. H. Jawad, A. Abdulhameed, N. Najwa, N. Abd Malek and Z. Alothman, Int. J. Biol. Macromol. 164 (2020). https://doi.org/10.1016/j.ijbiomac.2020.08.201
6. Z. Şenol, S. Çetinkaya, A. F. Yenidünya, F. Başoğlu-Ünal and A. Ece, Int. J. Biol. Macromol. 199 (2022). https://doi.org/10.1016/j.ijbiomac.2022.01.008
7. M. M. Abou Alsoaud, M. A. Taher, A. M. Hamed, M. S. Elnouby and A. M. Omer, Sci. Rep. 12, 12972 (2022). https://doi.org/10.1038/s41598-022-17305-w
8. A. Hosney, S. Ullah and K. Barčauskaitė, Mar. Drugs 20, 675 (2022). https://doi.org/10.3390/md20110675
9. Y. Boumezough, G. Viscusi, S. Arris, G. Gorrasi and S. A. C. Carabineiro, Int. J. Mol. Sci. 26, 6717 (2025). https://doi.org/10.3390/ijms26146717
10. T. Jadoon, K. Carter-Fenk, M. B. Siddique, J. Herbert, R. Hussain, S. Iqbal, J. Iqbal and K. Ayub, J. Mol. Liq. 297, 111902 (2019). https://doi.org/10.1016/j.molliq.2019.111902
11. E. Aziz, Y. Achour, M. el Himri, L. Rachid, and M. EL Haddad, Int. J. Environ. Anal. Chem. 103, 1 (2021). https://doi.org/10.1080/03067319.2021.1873306
12. R. Abdelmajid, H. Ben El Ayouchia, L. Rachid, S.-E. Stiriba, H. Anane and M. EL Haddad, Appl. Surf. Sci. 390 (2016). https://doi.org/10.1016/j.apsusc.2016.08.059
13. M. Bellaj, H. Yasid, K. Aziz, A. Regti, M. E. Haddad, M. E. Achaby, A. Abourriche, L. Gebrati, T. Agustiono Kurniawan and F. Aziz, Environ. Res. (2024). https://doi.org/10.1016/j.envres.2024.118352
14. R. Et-Tanteny, I. Allaoui, R. Haloui, S. Khattabi, K. Draoui and K. el khadiri, Chem. Phys. Impact 11, 100919 (2025). https://doi.org/10.1016/j.chphi.2025.100919
15. R. Mecheri, A. Zobeidi, S. Atia, S. Neghmouche Nacer, A. A. M. Salih, M. Benaissa, D. Ghernaout, S. A. Arni, S. Ghareba and N. Elboughdiri, Materials 16, 4082 (2023). https://doi.org/10.3390/ma16114082
16. H. Yazi, Z. Ammar, A. Douadi, E. Tidjani, D. Ghernaout, N. Elboughdiri, and Y. Moussaoui, J. Propul. Technol. 45, 475 (2024).
17. S. Bahemmi, A. Zobeidi, S. Atia, S. Neghmouche Nacer, D. Ghernaout and N. Elboughdiri, J. Propul. Technol. 44, 812 (2023). https://doi.org/10.52783/tjjpt.v44.i5.2678
18. A. Dalvand, R. Nabizadeh, M. R. Ganjali, M. Khoobi, S. Nazmara and A. H. Mahvi, J. Magn. Magn. Mater. 404, 179 (2016). https://doi.org/10.1016/j.jmmm.2015.12.040

19. H. Arabyarmohammadi, A. Khodadadi Darban, M. Abdollahy, R. Yong, B. Ayati, A. Zirakjou and Sjoerd E. A. T. M. van der Zee, J. Polym. Environ. 26, 2107 (2018). https://doi.org/10.1007/s10924-017-1102-6
20. M. Paredes-Laverde, M. Salamanca, J. D. Diaz-Corrales, E. Flórez, J. Silva-Agredo, R. A. Torres-Palma, J. Silva-Agredo and R. A. Torres-Palma, J. Environ. Chem. Eng. 9 (2021). https://doi.org/10.1016/j.jece.2021.105685
21. A. Kumar, P. Lingfa, Mater. Today Proc. 22, 737 (2020). https://doi.org/10.1016/j.matpr.2019.10.037
22. H. H. Murray, in Developments in Clay Science, Ed. by H. H. Murray, Vol. 2 (Elsevier, Amsterdam, 2006), Chap. 2, p. 7. https://doi.org/10.1016/S1572-4352(06)02002-2
23. D. L. Bish, Clays Clay Miner. 41, 738 (1993). https://doi.org/10.1346/CCMN.1993.0410613
24. C. Detellier and S. Letaief, in Developments in Clay Science, Ed. by F. Bergaya and G. Lagaly, Vol. 5 (Elsevier, Amsterdam, 2013), p. 707. https://doi.org/10.1016/B978-0-08-098258-8.00022-5
25. L. Wang and A. Wang, J. Hazard. Mater. 147, 979 (2007). https://doi.org/10.1016/j.jhazmat.2007.01.145
26. G. Crini and P. M. Badot, Prog. Polym. Sci. 33, 399 (2008). https://doi.org/10.1016/j.progpolymsci.2007.11.001
27. M. K. Uddin, Chem. Eng. J. 308, 418 (2017). https://doi.org/10.1016/j.cej.2016.09.029
28. B. Taşdelen, D. İ. Çifçi and S. Meriç, Polym. Bull. 79, 9643 (2022). https://doi.org/10.1007/s00289-021-03970-w
29. B. Saikia and G. Parthasarathy, J. Mod. Phys. 1, 206 (2010). https://doi.org/10.4236/jmp.2010.14031
30. K. V. Narayana Saibaba, Mater. Res. Found. 125, 87 (2022). https://doi.org/10.21741/9781644901915-4
31. A. H. Jawad and A. S. Abdulhameed, Colloids Surf. A 605, 125329 (2020). https://doi.org/10.1016/j.colsurfa.2020.125329
32. H. S. Vardikar, B. A. Bhanvase, A. P. Rathod and S. H. Sonawane, Mater. Chem. Phys. 217, 457 (2018). https://doi.org/10.1016/j.matchemphys.2018.07.014
33. N. Tu, J. Shou, H. Dong, J. Huang and Y. Li, Catalysts 7, 302 (2017). https://doi.org/10.3390/catal7100302
34. S. Benamer-Oudih, D. Tahtat, A. Nacer Khodja, B. Mansouri, M. Mahlous, A. E. Guittoum, and S. Kebbouche Gana, Environ. Sci. Pollut. Res. 31, 39976 (2024). https://doi.org/10.1007/s11356-023-27907-0
35. B. Abebe, H. C. A. Murthy and E. Zereffa, J. Encapsulation Adsorpt. Sci. 8, 225 (2018). https://doi.org/10.4236/jeas.2018.84012
36. L. Xu, J. Zhang, J. Ding, T. Liu, G. Shi, X. Li, W. Dang, Y. Cheng and R. Guo, et al., Minerals 10, 72 (2020). https://doi.org/10.3390/min10010072
37. M. Thommes, K. Kaneko, A. V. Neimark, J. P. Olivier, F. Rodriguez-Reinoso, J. Rouquerol, and K. S. W. Sing, Pure Appl. Chem. 87 (2015). https://doi.org/10.1515/pac-2014-1117
38. N. Abd Malek, A. H. Jawad, A. Abdulhameed, K. Ismail and B. Hameed, Int. J. Biol. Macromol. 146 (2020). https://doi.org/10.1016/j.ijbiomac.2020.01.020
39. K. Moazeni, M. Mirzaei, M. Baghdadi and A. Torabian, Water Air Soil Pollut. 234, 413 (2023). https://doi.org/10.1007/s11270-023-06406-5
40. H. M. Agha, A. H. Jawad, L. D. Wilson, H. A. Kazem and Z. A. ALOthman, Int. J. Phytoremediation (2026). https://doi.org/10.1080/15226514.2026.2627222
41. M. Awad, A. H. Jawad, A. Abdulhameed and M. S. Mastuli, Int. J. Biol. Macromol. 161 (2020). https://doi.org/10.1016/j.ijbiomac.2020.06.069
42. S. Lagergren, Zeitschr. f. Chem. u. Ind. der Kolloide 2, 15 (1907). https://doi.org/10.1007/BF01501332
43. Y. S. Ho and G. McKay, Chem. Eng. J. 70, 115 (1998). https://doi.org/10.1016/s0923-0467(98)00076-1
44. W. S. Ngah, L. C. Teong, and M. A. K. Megat Hanafiah, Carbohydr. Polym. 83, 1446 (2011). https://doi.org/10.1016/j.carbpol.2010.11.004
45. I. Langmuir, J. Am. Chem. Soc. 40, 1361 (1918). https://doi.org/10.1021/ja02242a004
46. J. Appel, Surf. Sci. 39, 237 (1973). https://doi.org/10.1016/0039-6028(73)90105-2
47. M. I. Temkin, Acta Physicochim. URSS 12, 327 (1940).
48. K. Y. Foo and B. H. Hameed, Chem. Eng. J. 156, 2 (2010). https://doi.org/10.1016/j.cej.2009.09.013
49. A. H. Jawad, A. S. Abdulhameed and M. S. Mastuli, J. Polym. Environ. 28, 1095 (2020). https://doi.org/10.1007/s10924-020-01671-5
50. M. N. V. Ravi Kumar, React. Funct. Polym. 46, 1 (2000). https://doi.org/10.1016/S1381-5148(00)00038-9
51. S. Hussain, M. Kamran, S. A. Khan, K. Shaheen, Z. Shah, H. Suo, Q. Khan, A. B. Shah, W. Ur Rehman, Y. O. Al-Ghamdi and U. Ghani, Int. J. Biol. Macromol. 168, 383 (2021). https://doi.org/10.1016/j.ijbiomac.2020.12.054
52. C. A. Demarchi, M. Campos and C. A. Rodrigues, J. Environ. Chem. Eng. 1, 1350 (2013). https://doi.org/10.1016/j.jece.2013.10.005
53. A. H. Jawad, A. S. Abdulhameed, A. Reghioua, Z. M. Yaseen, Int. J. Biol. Macromol. (2020). https://doi.org/10.1016/j.ijbiomac.2020.07.014
54. B. Tanhaei, A. Ayati, M. Lahtinen and M. Sillanpää, Chem. Eng. J. 259, 1 (2015). https://doi.org/10.1016/j.cej.2014.07.109
55. A. H. Jawad, N. S. A. Mubarak and A. S. Abdulhameed, J. Polym. Environ. 28, 624 (2020). https://doi.org/10.1007/s10924-019-01631-8
56. V. S. Munagapati, V. Yarramuthi and D.-S. Kim, J. Mol. Liq. 240, 329 (2017). https://doi.org/10.1016/j.molliq.2017.05.099
57. L. Zeng, M. Xie, Q. Zhang, Y. Kang, X. Guo, H. Xiao, Y. Peng and J. Luo, Carbohydr. Polym. (2015). https://doi.org/10.1016/j.carbpol.2015.01.021

58. A. H. Jawad, A. S. Abdulhameed, S. N. Surip and S. Sabar, Int. J. Environ. Anal. Chem. (2020). https://doi.org/10.1080/03067319.2020.1807966
59. M. Moharramnejad, R. E. Malekshah, S. Mohammadreza Mojab, M. Shahi, S. Gharanli, S. S. Mirbagheri, B. Mirtamizdoust and M. Mohammadkhani, J. Inorg. Organomet. Polym. Mater. 34, 1572 (2024). https://doi.org/10.1007/s10904-023-02894-4
60. R.EL Kaim Billah, A. Zaghloul, L. bahsis, N. A. Oladoja, Z. azoubi, A. taoufyk, H. majdoubi, J.S. Algethami, A. Soufiane, E. A. López-Maldonado, M. Wasilewska and N. Elboughdiri, Mater. Today Sustain. 25, 100660 (2024). https://doi.org/10.1016/j.mtsust.2023.100660
61. L. R. Domingo, E. Chamorro, and P. Pérez, J. Org. Chem. 73, 4615 (2008). https://doi.org/10.1021/jo800572a
62. X.-K. Wang, S. Yu, X. Wang, Y. Ai, X. Tan, T. Hayat and W. Hu, J. Mater. Chem. A 4 (2016). https://doi.org/10.1039/C6TA00890A

Abbreviations and notation:

MO, Methyl orange; ECH, epichlorohydrin; DFT, density functional theory; c-CTS, chitosan commercial; b-CTS, chitosan synthesized; CTS-KC ,kaolinite chitosan; c-CTS-ECH/KC, epichlorohydrin-crosslinked chitosan comercial/kaolinite biocomposites; b-CTS-ECH/KC, epichlorohydrin-crosslinked chitosan synthesized /kaolinite biocomposites; INRAA, National Institute of Agronomic Research of Algeria; RSM-BBD, Box-Behnken Design; XRD, X-ray diffraction; FTIR, Fourier transform infrared; BET, Brunauer–Emmett–Teller; SEM-EDX, energy-dispersive X-ray spectroscopy; UV–Vis, UV–Visible spectrophotometer; HOMO, Highest Occupied Molecular Orbital; LUMO, Lowest Unoccupied Molecular Orbital.